A Phenomenological Approach for Understanding the High Magnetic Coercivity State of a Fe–O Nanocrystalline Press Compact

J. Kargin[1], A. S. Lileev[2], Y. V. Konyukhov[2], D. G. Zhukov[2], H. Sanchez Cornejo[3,7], Ji Won Seo[4], S. N. Holmes[5], J. Albino Aguiar[6], C. H. W. Barnes[7], and L. De Los Santos Valladares[6,7]

[1]Department of Technical Physics, Faculty of Physics and Technical Sciences, NPJSC, L.N. Gumilyov Eurasian National University, Astana 010008, Kazakhstan
[2]Department of Physics and Materials Science, National University of Science and Technology "MISIS," 119049 Moscow, Russia
[3]Laboratorio de Cerámicos y Nanomateriales, Facultad de Ciencias Físicas, Universidad Nacional Mayor de San Marcos, 14-0149 Lima, Peru
[4]College of Science and Technology Convergence, Yonsei University, Wonju 26493, South Korea
[5]Department of Electronic and Electrical Engineering, University College London, WC1E 7JE London, U.K.
[6]Programa de Pós-Graduação em Ciências de Materiais, Centro de Ciências Exatas e da Natureza, Universidade Federal de Pernambuco, Recife 50670-901, Brazil
[7]Cavendish Laboratory, Department of Physics, University of Cambridge, CB3 0US Cambridge, U.K.

Experimentally obtained magnetic signals for a Fe–O nanocrystalline press compact were fitted using a phenomenological approach. This method considers the individual properties of microvolumes and their statistics. It also helps avoiding complex calculations while focusing on local fundamental magnetic characteristics without considering internal processes. Currently, the precise estimation of internal processes in local areas is nearly impossible. They depend on fluctuations in the anisotropy field, texture degree, and phase ratio. A cubic compact (10^3 mm^3 volume) was fabricated by pressing magnetite particles mixed with 20% iron by weight in a high-energy milling machine. After characterizing the compacts by X-ray diffraction (XRD), their magnetic signals were measured to obtain the saturation magnetization ($M_s = 0.97$ T), residual magnetization ($M_r = 0.456$ T), and coercivity ($H_c = 0.685$ kOe). The results suggest that the particle anisotropy fields relate to the effective anisotropy constants from the interaction between iron and magnetite particles. It is also found that single domains formed by iron particles contribute to high coercive states. This confirms that increasing the degree of texture results in an increment of the relative remanence and coercivity.

Index Terms— **Iron oxide, magnetic properties of materials, nanocrystalline powder, press compacts.**

I. Introduction

NOWADAYS, there is a big interest in developing novel magnets or improving the existing ones because of their various applications in energy storage, communication, medicine, and basic scientific research [1], [2], [3], [4]. In most cases, the discovery of novel magnets occurs empirically, based on the analysis of numerous experimental data, while the theoretical justification is often contradictory [5], [6], [7].

The classical Barnett theory suggests that the magnetization curve (magnetic induction versus magnetic field strength) can be described by the initial magnetization, coercivity, and remanence parameters [1], [2]. However, a better approach for understanding and predicting the magnetic properties of a material is the theory of micromagnetism, which includes the local distribution of the magnetic moments to the equation of the total energy for ferromagnets [1], [8], [9]. In other words, the micromagnetism theory considers microscopic domains to explain the magnetic behavior of bulk materials based on the interaction of elementary magnetic moments [1], [8], [9]. The theory describes well the processes of magnetization reversal, domain structure, coercive force, and magnetic susceptibility [1], [8], [9].

A disadvantage of the micromagnetism approach is the use of simplified models, which do not always reflect actual conditions in materials, i.e., it is limited to very small fields $\boldsymbol{H}$ and ideal crystals. In fact, real crystals have structural defects, such as impurity atoms, vacancies, dislocations, cracks, multiple phases, and so on, which make the modeling to be more complex. Besides, the micromagnetism theory does not consider the structure and properties of the domain boundaries, the orientation, or influence of the defects on the magnetic properties of the material, especially for polycrystalline materials. Consequently, there is still no understanding of the origin of effects, such as highly coercive states or magnetization reversal processes in hard magnetic materials.

In this work, we introduce a phenomenological approach considering the individual magnetic properties of microvolumes and their statistics to eliminate the need of precise calculations. The approach considers local fundamental magnetic properties without analyzing internal processes in the

Received 6 July 2025; accepted 7 July 2025. Date of publication 14 July 2025; date of current version 27 August 2025. Corresponding author: L. De Los Santos Valladares (e-mail: ld301@cam.ac.uk).

This article has supplementary material provided by the authors and color versions of one or more figures available at https://doi.org/10.1109/TMAG.2025.3587795.

Digital Object Identifier 10.1109/TMAG.2025.3587795

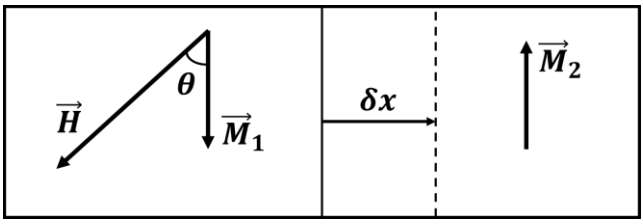

Fig. 1. Boundary separating two domains.

local regions. Since describing the hysteretic properties of real materials should be phenomenological, the present work compares the experimental hysteresis with the modeling for Fe–O alloys compacts with adequate criterion for the correctness solution.

II. Methodology

A. Theoretical Considerations

Within the framework of our phenomenological theory, a magnet is an ensemble of multi-domains, in which two processes occur under the influence of an external magnetic field: the reorientation of the magnetic moments of the individual domains in the direction of the external field and the displacement of the boundaries of neighboring domains [10].

The theory requires to know the exchange interaction constants, magnetic anisotropy constants, geometric constants of the sample, and angular dependences. For example, considering two neighboring domains with equal volumes, as represented in Fig. 1, $V_1 = V_2 = V$; in the absence of an external field, the sample is demagnetized ($M = 0$).

When an external field H is applied, the domain wall shifts to the right by δx. Thus, the condition for the stability of the new boundary position can be written as

$$\delta W_{\text{stab}} = \delta(W + W_H) = 0 \tag{1}$$

where $\boldsymbol{W}$ represents the energy of all internal magnetic interactions, and $\boldsymbol{W_H}$ is the energy of the magnet's interactions with an external field

$$\begin{aligned}\delta W_H &= -\left(\overrightarrow{M_1} - \overrightarrow{M_2}\right)\overrightarrow{H}\, S\delta x \\ &= -[M_S H\cos\theta - M_S H\cos(\pi - \theta)] \times S\delta x\end{aligned} \tag{2}$$

where $\overrightarrow{M_1}$ and $\overrightarrow{M_2}$ are the magnetizations of the neighboring domains, M_S is the saturation magnetization, $\boldsymbol{\theta}$ is the angle between vectors $\overrightarrow{M_1}$ and $\overrightarrow{H}$, and $\boldsymbol{S}$ is the area of the domain boundary.

From (1) and (2), we obtain

$$\delta W = -\delta W_H = 2M_S H(\cos\theta)S\delta x. \tag{3}$$

Hence, the field $H(x)$, for which the position of the domain wall at $\boldsymbol{x}$ is equilibrium, is given by

$$H(x) = \left(\frac{\partial W}{\partial x}\right)\frac{1}{2SM_S\cos\theta}. \tag{4}$$

A displacement of the domain wall by an amount $\partial\boldsymbol{x}$ will cause the appearance of magnetization in the sample

$$\delta M = 2M_S(\cos\theta)\frac{\delta V}{V} = \frac{2M_S(\cos\theta)S\cdot\delta x}{V}. \tag{5}$$

From (4) and (5), the magnetic susceptibility can be obtained

$$\chi = \frac{\partial M}{\partial H} = \frac{(2SM_S\cos\theta)^2}{V\frac{\partial^2 W}{\partial x^2}}. \tag{6}$$

For reversible displacements of the domain wall, the quasi-elastic force $\boldsymbol{W}$ energy is defined as

$$W = \gamma\cdot x^2$$

where γ is the elasticity coefficient of the domain boundary. Then

$$\chi = \frac{(2SM_S\cos\theta)^2}{\gamma\cdot V}. \tag{7}$$

In a previous work [10], the calculation of the interaction energy of the domain wall in Sm–Co–Cu–Fe–Zr alloys was reported considering the specific crystal structures that arise in the alloy after optimal heat treatment. For the critical field of domain wall separation, the following expression was provided:

$$H_c = \sqrt{2A/\pi M_S} \tag{8}$$

where $\boldsymbol{A}$ is the matrix anisotropy constant and $\boldsymbol{M_S}$ is the saturation magnetization of the sample.

Substituting the corresponding values $\boldsymbol{A} = 2\times10^6$ J/m^3 and $\boldsymbol{M_S} = 0.85$ G, the value $\boldsymbol{H_c} = 13.8$ kOe is obtained, which is twice the experimental value of $\boldsymbol{H_c}$ [11].

The processes of magnetization reversal and magnetic hysteresis of hard magnetic materials are irreversible generating magnetic hysteresis caused by [10] as follows: 1) delay in shifting domain boundaries; 2) delay in the formation of a stable magnetization reversal nucleus; and 3) irreversible processes of rotation of the magnetization vector in single-domain particles. Crystalline particles, as main components in real materials, can serve as the basis for modeling the processes of magnetization of materials. The particle volume is taken to be the volume contained between the positions of the domain wall before and after its displacement. It is assumed that the geometric shape of the particles does not affect the calculations. The proposed technique for modeling an ensemble of particles makes it possible to display the magnetization of microvolumes using arrows and the direction of magnetization of the microvolume, whereas the length indicates the contribution of this microvolume to the total magnetization.

Fig. 2 shows the schematically change of the magnetization in a cubic piece (microvolume) of the material under the influence of an external field, acting parallel to the Z-axis in both negative and positive directions. If the microvolume is in a multi-domain state, then the magnetization vector $\boldsymbol{M}$ is directed parallel to the easy magnetization axis. When the magnitude of the magnetization vector ($\boldsymbol{M/M_S}$) reaches its maximum value (saturation magnetization), the microvolume becomes a single-domain state [Fig. 2(a)]. As the field increases, the direction of the magnetization vector of the microvolume begins to change, but its length remains constant, as shown in Fig. 2(b).

The angle $\boldsymbol{\theta}$ between the Z-axis and the direction of the magnetization vector is calculated by

$$\cos\theta = \frac{M}{M_S} \tag{9}$$

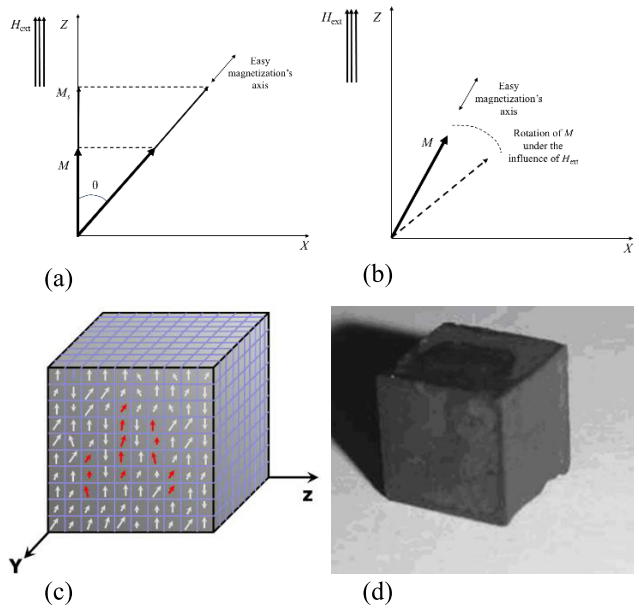

Fig. 2. Schematic representation of changes in the magnetization in a microvolume in a multi-domain state. (a) Change in the length of the arrow (vector of magnetization) with increasing the external field. (b) Rotation of the arrow as the external field increases. (c) Diagram of a model ensemble of microvolumes. Microvolumes are arranged in the form of cubes (the arrows indicate the magnetic moments for the microvolumes). (d) Photography of the press compact obtained by high-energy milling of Fe–O powder.

where $\boldsymbol{M}$ is the projection of the magnetization vector onto the Z-axis and $\boldsymbol{M_S}$ is the module of the saturation magnetization vector.

The magnetocrystalline texture of an ensemble of microvolumes is determined considering the value of the angle θ. If all the microvolumes in the ensemble have an angle θ equal to zero, then such an ensemble is considered perfectly textured. If the angle is uniformly distributed over the interval from 0° to 90°, the ensemble is called isotropic.

Based on the above, Fig. 2(c) presents a model of a permanent magnet of the Fe–O system studied in this work. The ensemble contains 1000 particles (microvolumes measuring 10 × 10 × 10), each one with a single-domain structure and their own critical domain wall separation field ($\boldsymbol{H_{cr}}$). Under external magnetic fields lower than $\boldsymbol{H_{cr}}$, magnetization microvolume does not occur. With an external field $\boldsymbol{H} > \boldsymbol{H_{cr}}$, the domain walls are separated, which corresponds to the magnetization of the ensemble due to the growth of some domains, whose magnetic moments make smaller angles with the direction of the external field due to other domains whose angles are greater than 90°.

The key of the technology for producing press-compact powder magnets is grinding an alloy with the right stoichiometric composition. This alloy is ground to an average particle size less than 5 μm. This process helps achieve a nearly single-domain state. Grinding $SmCo_5$ alloys increases its coercive force to 15 kOe, which is 5–10 times stronger than typical values in alloys of the Fe–Ni–Co–Fe–Ti system [12].

B. Modeling

The interaction of particles was not considered for modeling the magnetization processes. The initial parameters of the ensemble were selected in a way that the experimental and calculated hysteresis loops coincide. The saturation field of the microvolume $\boldsymbol{H_S}$, the angle $\boldsymbol{\theta}$ between the direction of the external field and the light axis of the microvolume, and the critical field of detachment of the domain wall from the pinning site $\boldsymbol{H_{cr}}$ were taken as variable. The results of the modeling were compared with experimental data for Fe–O alloys.

A microvolume was defined as the part of the material having a given set of parameters. The crystalline anisotropy value is considered constant and, consequently, the anisotropy field of the material and the saturation magnetization $\boldsymbol{M_S}$ are constant for the entire volume. The magnitude of the magnetostatic interaction field was determined using the method proposed in [12], [13], and [14]. In brief, the h_i field for a magnetostatic interaction acting on the ith microvolume was calculated using the formula

$$h_i = h + \frac{3}{4\pi} \sum_{j=1(j\neq 1)}^{n} m_i F_{ij} \tag{10}$$

where F_{ij} is the coefficient of interaction computed in [12]. Also, $m_i = M_i/M_s$ and $h = (H/H_s) = 3H/4\pi M_s$, where H is the external field and m_i is the saturation magnetization of the ith microvolume.

Following the theory of micromagnetism to study the magnetic properties of a bulk material, a continuum system or magnetics is replaced by a set of discrete interacting subsystems in the form of individual microvolumes or cubes [see Fig. 2(c)]. In this approach, one of the main problems for mathematical representation is to derive differential equations for the magnetization field. The cubes are assumed to be small enough, so that the magnetization can be assumed constant ($\boldsymbol{M_S}$ value) within each cube but can vary from cube to cube. This approach is often used in numerical methods, such as the finite element method (FEM) or the finite difference method (FDM) to solve the problems in electromagnetism and other areas of physics [9]. For example, it helps to determine the magnetic field distribution in a homogeneous material. In this approach, the general equation for the magnetization $\boldsymbol{M}$ is

$$\nabla^2 \overrightarrow{M} = -\mu_0 \overrightarrow{H} \tag{11}$$

where $\boldsymbol{\mu_0}$ is the magnetic permeability.

For the 1-D case, this equation can be written as

$$\frac{d^2 M(x)}{dx^2} = -\mu_0 H(x). \tag{12}$$

Furthermore, introducing a discretization grid with step Δx

$$x_i = i\,\Delta x. \tag{13}$$

Then, at point $\boldsymbol{x_i}$, the approximation of the second derivative becomes

$$\frac{M_{i+1} - 2M_i + M_{i-1}}{\Delta x^2} = -\mu_0 H_i. \tag{14}$$

This difference operator leads to a system of linear equations for the values of $\boldsymbol{M_i}$

$$M_{i+1} - 2M_i + M_{i-1} = -\mu_0 H_i (\Delta x)^2. \tag{15}$$

By solving the system of linear (15) for each discrete ith element, the corresponding $\boldsymbol{M_i}$ values are determined for the 1-D case.

Similarly, for the 3-D case in the form of cube, the system of linear equations is obtained by the following equation introducing a discretization grid with step for each regarding axis: $\Delta x = \Delta y = \Delta z$ and following the approximation of the second derivative:

$$\begin{cases} M_{i+1} - 2M_i + M_{i-1} = -\mu_0 H_i (\Delta x)^2 \\ M_{i+1} - 2M_i + M_{i-1} = -\mu_0 H_i (\Delta y)^2 \\ M_{i+1} - 2M_i + M_{i-1} = -\mu_0 H_i (\Delta z)^2. \end{cases} \tag{16}$$

The magnetostatic interaction field is incorporated using a mean-field approximation described by Schabes and Aharoni [12], where each microvolume experiences a demagnetizing field $H_{\text{demag}} = NM$, where N is the demagnetization factor determined from the geometry of the ensemble. This is consistent with the method described by Schabes and Aharoni [12] for the arrays of ferromagnetic cubes and extended in [13] and [14].

The modeling program employs the fundamental package NumPy in Phyton in order to solve the system of linear equations. The *solve banded* function in Python is used to solve a system of linear equations in the form

$$Ax = b \tag{17}$$

where A is the banded matrix and b corresponds to the right-hand from (16)–(18) linear equations (see diagram block program in Fig. S1). A is defined as a tridiagonal matrix in the program, as noted in Fig. S2.

With the aim to model the $10 \times 10 \times 10$ cubic permanent magnet (ensemble of 1000 microvolumes), the discretizational step size is defined as

$$\Delta x = \Delta y = \Delta z \rightarrow dx = dy = dz = 1. \tag{18}$$

Eventually, to plot the dependence of the magnetization $\boldsymbol{M}$ on the field $\boldsymbol{H}$, the phenomenological model of reverse magnetization (PMRM) can be used (see [15] and Supporting Material S1 and S2).

III. Experiment

A. Sample Preparation

A mixture of hematite (α-Fe_2O_3, 80%) and iron (α-Fe, 20%) powder was milled during 4 h in an AGO-2U high-energy planetary type ball milling with two sealed drums. No process control agent (PCA) was used. The balls have a diameter of (3–6) mm made of ShKh15 steel, 200 g into each drum. The ratio of the mass of balls to the powder mass was 10:1. The powder was pressed with a maximum load of 20 T using a separable titanium compression mold. Alcohol was added during compacting in a special cuvette to enhance powder uniformity. No additional binder was used. The resulting press compact had the shape of cube with dimensions of (10.0 ± 0.2) mm. A photography of the pressed-compact is shown in Fig. 2(d).

The heating and thermomagnetic treatment (TMT) processes were performed in air following the same procedure reported in [7] and [16]. In brief, a homemade installation consisting of an electric resistance furnace and an electromagnet, using a process activation setting (Ustanovka Aktivacii Processov, UAP-3, in Russian) magnetic mill (see Fig. S3). The magnetic field strength between the concentrators was about 8000 kA/m in a 10 mm gap. Heat treatment in air was carried out using the same installation, but without turning on the electromagnet. A magnetic system of $SmCo_5$ permanent magnets and a magnetic conductor yoke was used for TMT in air. The temperature was maintained and controlled using VRT and KSP-4 devices and a chromel–alumel thermocouple XA with an accuracy of ± 2 °C.

In the present work, the powder was compacted in the presence of a magnetic field to obtain a crystalline texture that allows for a residual induction of 9–10 kG. The press compact was subsequently annealed at 1120 °C for 40 min. The temperature then decreases to 850 °C at a rate of 1.5 °C/min and holds at this temperature for 20 min. The sample was then cooled to room temperature at a rate above 150 °C/min. This technology is currently widely used in the production of permanent magnets by powder metallurgy [17], [18].

B. Measurements

The X-ray diffraction (XRD) patterns of the sample were obtained using a DRON-4-07 diffractometer. A tube with a cobalt anode [radiation wavelength $\lambda K_{-\alpha av} = 0.179021$ nm (1.79021 Å)], in tube operating mode $U = 40$ kV, $I = 30$ mA; slots: 8 mm (from the tube), 1 mm (reception on the circumference of the goniometer), 1 mm (in front of the counter); monochromator C (graphite). The range of diffraction angles 2θ varied from 20° to 80° with 2°/min speed and Bragg–Brentano configuration. Phase qualitative and quantitative analyses were carried out according to the standard technique. For quantitative phase analysis, the X-ray program (PHAN%) was used [19]. This program is a modification of the Rietveld method [20] as it does not require to specify the coordinates of atoms in the crystal lattice. According to it, the experimental spectrum is described by the sum of polynomial background and the theoretical spectra of phases weighted by their volume fractions. During the calculation, the program refines the lattice periods and the fine crystal structure parameters. This includes the size of coherent scattering regions and the magnitude of the root mean square (rms) microstrain. It also considers the imaging geometry and various alignment parameters. The program allows to take into account the influence of texture, which makes it possible not only to calculate the volume fractions of phases but also to determine the crystallographic texture (pole densities). One of the important features of the quantitative analysis is the ability to determine the content of amorphous phase in amorphous-crystalline objects.

The qualitative phase analysis was carried out according to the standard technique, i.e., identification of the substance in the mixture is carried out by a set of its interplanar distances d. For this purpose, the determination of reflection angles θ and interplanar distances is carried out from X-ray radiographs

according to the Wolf–Bragg law using the following equation:

$$d = \frac{n\lambda}{2\sin\theta} \tag{19}$$

where n is the reflection order, d is the interplanar distance (in m), λ is the wavelength of the used radiation (in m), and θ is the diffraction angle (in degrees).

Relative error of diffraction angle measurement is calculated by the formula

$$\frac{\Delta a}{a} = \frac{\cot\theta}{\Delta\theta} \tag{20}$$

where Δa is the absolute error of period measurement (%) and $\Delta\theta$ is the absolute error of diffraction angle determination (rad). The absolute error of the lattice period measurement is 3×10^{-5} nm.

The average particle size D was calculated using the Scherrer formula

$$D = \frac{0.94\lambda}{\beta\cos\theta} \tag{21}$$

where β is the true physical line broadening of the investigated sample calculated by the method of approximation and Fourier analysis, in radians. The goodness-of-fit parameter (χ^2) was calculated based on the residual sum of squares between the experimental and modeled XRD intensities. Using the PHAN% software, χ^2 was determined using the formula

$$\chi^2 = \frac{\sum\left[(I_{\text{obs}} - I_{\text{calc}})^2/\sigma^2\right]}{(N-P)} \tag{22}$$

where I_{obs} and I_{calc} are the observed and calculated intensities, respectively, σ is the standard deviation, N is the number of data points, and P is the number of refined parameters. Goodness-of-fit $\chi^2 \approx 1.35$ indicates a statistically reliable fit for the refined model.

The magnetic properties were measured by using a Lake Shore Cryotronics VSM 7400 vibration sample magnetometer (USA). The coercive field ($\boldsymbol{H_C}$), residual magnetization ($\boldsymbol{M_r}$), and saturation magnetization ($\boldsymbol{M_S}$) were recorded. The error in determining the magnetic moment was 10^{-6} A $\times$ m^2. The microstructure of the powder was studied using a scanning electronic microscope SEM Hitachi S-4100 (Japan).

IV. Results and Discussion

A. Microstructure and Structural Characteristics

Fig. 3(a) shows the micrography obtained by SEM of the initial powder before processing in high-energy milling. The original particle size of the powder is 45 μm in average. During intensive milling with high rotation speeds, strong friction between particles occurs, accompanied by localized temperature increases, resulting in the metallic iron to directly oxidize to hematite

$$4\text{Fe} + 3\text{O}_2 \rightarrow 2\text{Fe}_2\text{O}_3.$$

The XRD pattern obtained before grinding [see Fig. 4(a)] shows that the initial state of the press compact consists entirely of hematite–iron oxide α-Fe_2O_3 with a lattice of type D5.1, hR10, $a = 0.5034$ nm, and $c = 1.3747$ nm (in hexagonal coordinate system) [21], [22], [23].

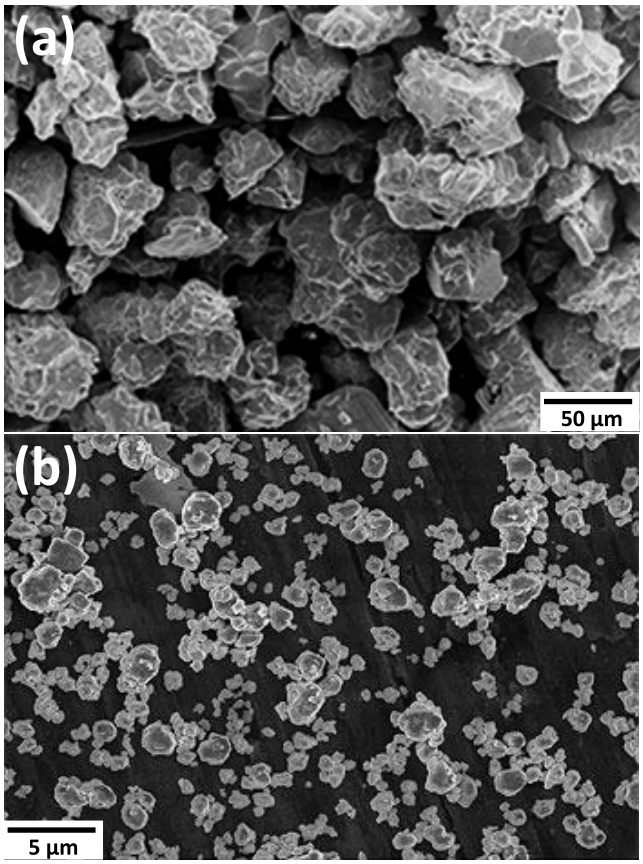

Fig. 3. SEM images (a) initial sample and (b) sample processed in high-energy mill during 4 h.

TABLE I
Phase Analysis by XRD From the Initial Sample (Press Compact) and After 4 h Grinding Process

Grinding time (h)	Phase composition	χ^2	Volume (%)	D (nm)
Initial	Hematite Fe_2O_3	1.35	100	-
4	Hematite Fe_2O_3	1.35	2	-
	Magnetite Fe_3O_4		80	150
	Wustite FeO		2	61
	α-Fe		16	70

Fig. 2(d) shows the press compact obtained after high-energy milling Fe–O powders. The shape of the pressed compact is cubic with lateral side (10.0 $\pm$ 0.2) mm. Fig. 3(b) shows the SEM micrograph of the crushed pressed compact obtained after 4 h grinding process.

Fig. 4(b) shows the XRD pattern of the press compact after 4 h of grinding process under high-energy milling. The average values of the block sizes calculated by Scherrer's technique (21) after grinding for 4 h were 150, 61, and 70 nm for Fe_3O_4, FeO, and α-Fe, respectively. The obtained material is nanocrystalline (see the crystallite size in Table I).

Mechanical activation, typically through high-energy ball milling, induces this transformation by introducing defects and increasing the internal energy of the hematite particles.

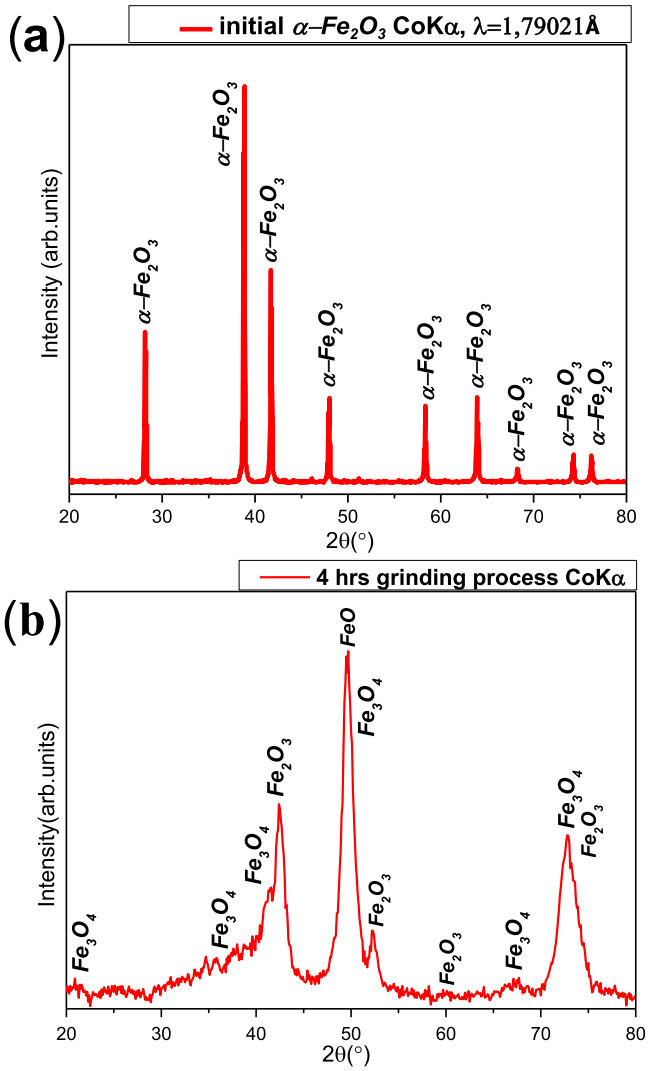

Fig. 4. XRD patterns (a) initial sample and (b) sample processed in high-energy mill during 4 h.

The process leads to a significant change in their structural and phase state. After a 4 h treatment, the amount of α-Fe is 16%, while hematite decreased and Fe_3O_4 (about 80%) and FeO phases appeared. The phase transformation of hematite (α-Fe_2O_3) to magnetite (Fe_3O_4) during mechanical milling is well described in [24], [25], and [26].

The XRD pattern obtained after 4 h of treatment is hugely different from the XRD pattern obtained before grinding. Additional to the lines of the Fe_2O_3 phase detected, at the same time, the peak characteristic of two other iron oxides appear: FeO, with the $B1$ structure, and Fe_3O_4 with the $H1.1$ lattice. Weak lines from α-Fe ($A2$) are also visible, indicating the appearance of a small amount of this phase. Compared to the first diffraction pattern before grinding process, the lines in the second XRD pattern are broadened. This suggests that the size of crystallites in the powder sharply decreases and strong distortions of the crystal lattice of phases also appear due to intense plastic deformation. XRD results are presented as separate, indexed figures, facilitating clearer phase identification. Peaks corresponding to Fe_3O_4 (magnetite), FeO (wüstite), and α-Fe were observed after milling, indicating transformation from initial hematite.

The results of quantitative phase analysis of XRD data were calculated and presented in Table I. The goodness-of-fit $\chi^2 \approx 1.35$ is shown for both cases.

Based on the data of phase and XRD analysis data, we can deduce that the phase composition of the powder, initially consisting of Fe_2O_3 oxide, changes during grinding according to the following scheme (the structural type of phases is indicated in parentheses):

$$\mathrm{Fe_2O_3}(D5.1) \rightarrow \mathrm{Fe}(A2) + \mathrm{Fe_2O_3}(D5.1) + \mathrm{Fe_3O_4}(H1.1) + \mathrm{FeO}(B1).$$

The formation of Fe_3O_4 (magnetite) during high-energy ball milling is primarily driven by mechanochemical reduction of hematite (α-Fe_2O_3) and reaction with metallic Fe, both promoted by mechanical impacts and localized thermal spikes. During milling, repeated collisions of the steel balls generate shear forces and local temperatures exceeding 400 °C–500 °C, sufficient to partially reduce Fe^{3+} in hematite to a mixed-valence Fe^{2+}/Fe^{3+} state, favoring Fe_3O_4 formation. Additionally, metallic Fe introduced as a starting component and further enriched by abrasion of steel media participates in redox reactions, converting hematite into magnetite via

$$3(\alpha\text{-}\mathrm{Fe_2O_3}) + \mathrm{Fe} \rightarrow 4\mathrm{Fe_3O_4}.$$

This process aligns with previous reports on mechanically induced phase transformations in iron oxides [24], [25], [26], [27] explains the dominant Fe_3O_4 phase observed in the XRD pattern after 4 h of milling.

Therefore, it was shown that the process of grinding powders in a high-energy planetary ball mill leads to a change in the initial phase composition. Such high-energy ball milling of powders is called the mechanical alloying method and is well described in a review by Koch and Whittenberger [28]. The mechanical alloying method involves the synthesis of materials by their high-speed milling, which occur due to phase transformations caused by dispersion processes. As a result of such processing, a cellular dislocation structure is formed inside the powder particles, which leads to the formation of randomly oriented "blocks" separated from each other by high-angle boundaries, i.e., nanocrystalline grains [10]. This, in turn, leads to changes in the magnetic properties of the obtained samples.

For the case of grinding hematite powders, the change in the values of the coercive force and magnetization of the material is primarily due to dispersed particles α-Fe [29], [30].

Thus, the principal possibility of obtaining a magneto-solid composite material with nanocrystalline structure in the Fe–O system has been demonstrated.

This study shows that although the size of the starting powder component was in the order of microns, high-energy milling for 4 h was enough to shrink the crystallite size to the nanometer scale. This was confirmed by SEM micrographs [Fig. 3(b)] and the Scherrer calculus in the XRD analysis [see Fig. 4(b) and Table I]. Specifically, the Fe_3O_4 and α-Fe crystallites decrease size after the powder is crushed, milled, and pressing processes; 4 h of high-energy milling was enough

TABLE II
MAGNETIC PROPERTIES OF Fe/Fe_3O_4 OBTAINED BY HYSTERESIS LOOPS FOR THE 20%Fe + 80%Fe_3O_4 PRESS COMPACT AFTER 4 h GRINDING PROCESS (EXPERIMENTAL DATA) AND CALCULATED USING THE PMRM PROGRAM (MODELING RESULTS)

Magnetic properties	Experimental data	Fe/Fe_3O_4 (modelling results)					
		5/95	10/90	20/80	30/70	40/60	50/50
H_c (kOe)	0.685	0.581	0.568	0.648	0.722	0.884	0.953
M_r (T)	0.456	0.53	0.499	0.494	0.518	0.543	0.513
M_s (T)	0.97	0.97	0.99	0.976	1.004	1.035	0.989

to obtain the crystallite sizes of ∼70 nm for α-Fe and ∼61 nm for FeO. These sizes are consistent with the established single-domain size limits for these phases.

This supports our interpretation that the enhanced coercivity arises from single-domain particles, consistent with micromagnetic theory and previous experimental results in mechanically alloyed systems [31], [32].

B. Magnetic Analysis

The magnetic properties, such as coercivity, residual magnetization, and saturation magnetization, of the obtained press compact processed during 4 h in high-energy mill, were determined from hysteresis loops. The experimental results show that the saturation magnetization reaches 0.97 T, the residual magnetization is 0.456 T, and the coercive force is 685 Oe (see Table II). The experimental loops are typical of materials with a single magnetic phase.

To fit the experimental data, as well as to find out which phase in the annealed powder is responsible for the high coercive state of the material, an ensemble of particles simulating the Fe/Fe_3O_4 mixture was considered following the phenomenological modeling described above. Since α-Fe and Fe_3O_4 have different magnetic crystallographic anisotropy constants in magnitude and sign, the possible relations of the anisotropy fields of the phases were calculated from the experimental data. The program was adjusted to vary the parameters of the ensemble particles and, thus, to achieve the magnetic properties of the ensemble that corresponds to the experimental material. In this way, the magnetic behavior was analyzed by comparing the hysteresis loops. The experimental loop was recorded on a hysteresis graph with a recorder in a field of 5 kOe, the data of which were loaded into the PMRM program.

Fig. 5 shows both experimental and calculated hysteresis curves for the Fe/Fe_3O_4 system, based on the following change in the phase ratio, in %: Fe/Fe_3O_4 = (5/95), (10/90), (20/80), (30/70), (40/60), and (50/50). Changing the phase ratio (with other parameters unchanged) affects the properties of the ensemble: an increase in the Fe fraction leads to a monotonic increase in the coercivity (from 581 Oe at a Fe fraction of 5% to 953 Oe at Fe 50%). On the other hand, the increase in the Fe fraction does not significantly affect other magnetic

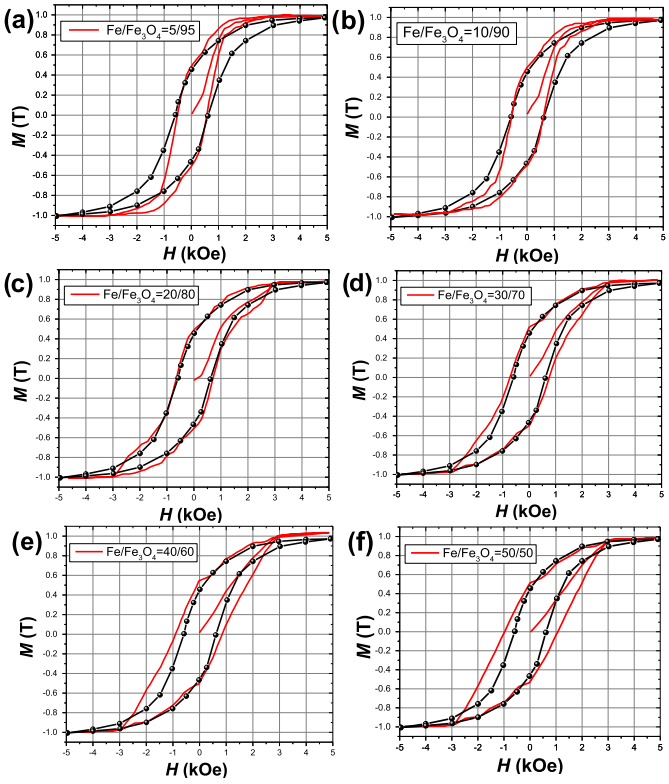

Fig. 5. Comparison of hysteresis loops for different Fe/Fe_3O_4 contains. The black points are experimental data obtained for 20%Fe + 80%Fe_3O_4 press compact and the red lines are calculated loops using a PMRM program, based on the change in the phase ratio (in %) for Fe/Fe_3O_4: (a) 5/95, (b) 10/90, (c) 20/80, (d) 30/70, (e) 40/60, and (f) 50/50.

characteristics, such as residual magnetization and saturation magnetization, which is evident from the data in Table II and Fig. 6.

When using the PMRM program, it was assumed that the texture value $A = 0.35$, where $A = (B_r^{\parallel} - B_r -)/B_r^{\parallel}$, which corresponded to the experimental conditions. Here, $B_r^{\parallel}$ is the residual magnetic induction when the external magnetic field is applied parallel to the sample plane, whereas $B_r^{\perp}$ is perpendicular to the sample plane.

Table II and Fig. 6 present the values of the coercive force H_C, residual magnetization M_r, and saturation magnetization M_S obtained from calculated data for each composition.

A comparison of the experimental hysteresis loop from compact after 4 h grinding process with the calculated ones shows their satisfactory agreement. Some discrepancy is explained by the fact that when the phase ratio changes, the effective anisotropy constants also change, which contributes to the change in magnetic properties, which was not considered in the modeling.

For example, for the sample Fe/Fe_3O_4 = 20/80, the experimental value of coercivity (0.685 kOe) is close to, but slightly higher than, the calculated value (0.648 kOe, see Fig. 6). This discrepancy arises from simplifications in the model: it uses fixed anisotropy constants and does not fully account for the magnetoelastic or interparticle exchange interactions present in real samples. Similarly, the experimental value of remanence [M_r (T) = 0.456 T] is slightly lower than the modeled one (0.494 T). This may be due to imperfect texturing in the

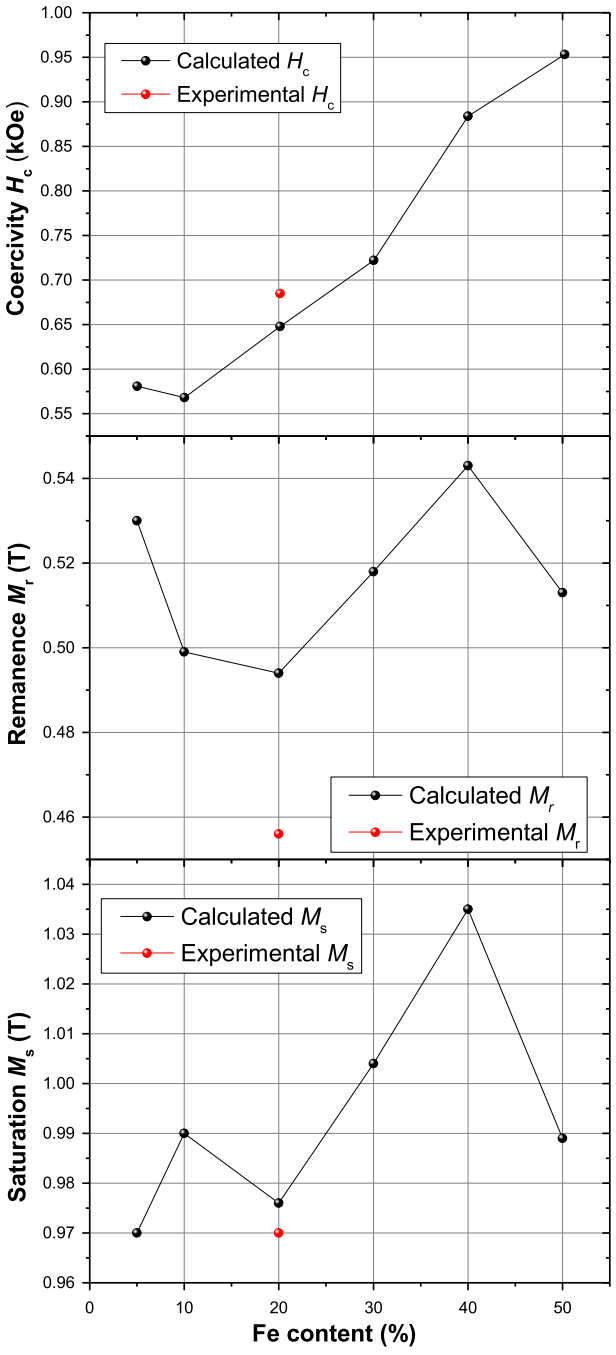

Fig. 6. Dependence of magnetic characteristics on iron content in the Fe/Fe_3O_4 system from calculated and experimental data.

real sample. The modeling assumes a Gaussian distribution of magnetization angles with a defined texture parameter ($A = 0.35$). Remarkably, for the saturation magnetization M_s (T), the experimental and calculated values match well (~0.97 T), suggesting that this phase ratio reflects more accurately the real composition. Thus, changing anisotropy fields also greatly affects the magnetic properties of the ensemble. A simultaneous increase in the anisotropy fields of both phases, which corresponds to an increase in the proportion of iron, leads to an increase in the coercive force. The residual magnetization does not change. Also, the magnitude of the saturation field

TABLE III
COMPARATIVE OF MAIN MODELING ASPECTS BETWEEN PMRM APPROACH AND TCMH MODEL

Property	This work (Fe/Fe_3O_4 composites)	Taurines et al. [33] – Hard Magnets (NdFeB)	Taurines et al. [33] – Soft Magnets (FeSi)
Modelling approach	Phenomenological (PMRM)	Thermodynamically consistent hysteresis model (TCMH)	
Coercivity H_c (kOe)	~0.648–0.953 (modelled), 0.685 (experimental)	~5,65	~0.001
Remanence M_r (T)	~0.456 (experimental)	~1.0–1.2	~1.5
Saturation magnetization M_s (T)	~0.97	~0.615	~0.992
Minor loop modelling	Not considered	Included and validated	Included
Target applications	Nanostructured Fe-O composites	Motors, permanent magnet systems	Transformers, electrical steels

increases. A simultaneous decrease in the anisotropy fields for both phases leads to a decrease in the coercive force and a decrease in the saturation field.

Also, the PMRM program shows that the values of residual magnetization and coercive force directly depend on the degree of texture of the material. By setting the misorientation angle with a Gaussian distribution with a mean value of 0 and reducing the dispersion to 70, then the coercive force increases to ~0.8 kOe; and the relative remanent magnetization reaches 0.68 T.

C. Comparison With Recent Hysteresis Models

A relevant comparison can be drawn between our phenomenological approach and other recent works. For example, Taurines et al. [33] developed a thermodynamically consistent magnetic hysteresis (TCMH) model applicable to both soft and hard magnetic materials. While their model emphasizes energy-consistent treatment of irreversible magnetization processes and reproduces full and minor loops accurately, our approach focuses on polycrystalline nanocomposites, where grain orientation, domain interactions, and local anisotropy distributions are dominant. Our model captures the coercivity enhancement due to nanoscale structuring and texture in oxide composites, whereas the TCMH model aims to accurately reproduce hysteresis behavior in bulk and advanced commercial magnetic alloys. The two approaches thus complement each other in their scope and applicability.

Our findings also match well with other ones recently reported in the literature. For example, Lileev et al. [29] reported coercivities in the range of 0.5–0.7 kOe for nanocrystalline $Fe–Fe_2O_3$ systems prepared by similar mechanical

activation techniques. Similarly, Gutfleisch et al. [31] and Fiorani [32] describe coercivity enhancements in Fe-based composites attributed to nanoscale domain formation and particle isolation. The observed saturation magnetization (0.97 T) and remanence (0.456 T) in our samples are also comparable to those for mechanically alloyed Fe–oxide systems with similar phase ratios. These results also confirm that nanostructuring and controlled texturing are effective strategies for improving magnetic performance in oxide-based hard magnetic materials. A comparative summary is presented in Table III.

V. Conclusion

A phenomenological approach to model the hysteresis loops of Fe–O nanocrystalline press compacts has been reported. Iron oxide compact has been fabricated via high-energy ball milling, following TMT. XRD and SEM analyses confirm the formation of magnetite (Fe_3O_4), α-Fe, and FeO phases, with crystallite sizes ranging from 60 to 710 nm. Mechanochemical reactions and thermal effects during milling promoted the partial reduction of hematite and the formation of ferromagnetic phases, particularly Fe_3O_4 and α-Fe. Magnetic measurements revealed enhanced coercivity (0.685 kOe), remanence (0.456 T), and saturation magnetization (0.97 T), promoted by the emergence of single-domain α-Fe grains and the development of crystallographic texture. The experimental coercivity values are similar to nanocrystalline Fe–oxide systems reported in the literature. The phenomenological model successfully simulates the hysteresis loops of the Fe/Fe_3O_4 mixtures of different composition rates. The modeling assumes uniform anisotropy and simplified magnetostatic interactions and results in closely experimental and theoretical match. The discrepancies between the measured and calculated loops are attributed to microstructural inhomogeneities, localized stress, and incomplete texture alignment, which are not considered in the model. A detailed treatment of magnetostatic interactions and finite-difference discretization has been provided to enhance the model reproducibility. Overall, this study demonstrates that high coercivity and tailored magnetic properties can be achieved in Fe–O composites through phase engineering, nanoscale control, and thermomagnetic alignment, whereas the proposed modeling approach serves as a predictive and interpretive tool for optimizing magnetic behavior in nanocrystalline oxide systems without relying on rare-earth elements.

Contribution Statement

Data acquisition, methodology, data curation, and formal analysis (J. Kargin, H. E Sanchez Cornejo, Y. V. Konyukhov, A. S. Lileev, and D. G. Zhukov), conceptualization, interpretation, validation, data curation, and visualization (Ji Won Seo, S. N. Holmes, J. Albino Aguiar, C. H.W. Barnes, and L. De Los Santos Valladares), and all authors have contributed in writing this article.

Acknowledgment

This work was supported in part by the PROFESSOR VISITANTE Program No. 13/2022 of the Universidade Federal de Pernambuco, Brazil, under Contract 019063/2023-39. H. Sanchez thanks the Peruvian Council of Science and Technology, CONCYTEC, for supporting this research through under Grant PE501083676-2023-PROCIENCIA.

J. Kargin would like to thank the JSC "Center for International Programs" of the Republic of Kazakhstan under the International Programme "500 scientists," Agreement for Scientific Internship No. 7971 dated July 2023. J. Albino Aguiar would like to thank CNPQ, Brazil, for supporting his research project.

References

[1] H. Gleiter, "Nanocrystalline materials," *Prog. Mater. Sci.*, vol. 33, no. 4, pp. 223–315, 1989, doi: 10.1016/0079-6425(89)90001-7.

[2] T. Xie and J. C. Grossman, "Crystal graph convolutional neural networks for an accurate and interpretable prediction of material properties," *Phys. Rev. Lett.*, vol. 120, no. 14, Apr. 2018, Art. no. 145301, doi: 10.1103/physrevlett.120.145301.

[3] A. S. Lileev, A. A. Parilov, and V. G. Blatov, "Properties of hard magnetic Nd–Fe–B films versus different sputtering conditions," *J. Magn. Magn. Mater.*, vols. 242–245, pp. 1300–1303, Apr. 2002, doi: 10.1016/s0304-8853(01)01269-0.

[4] W. F. Brown and A. E. LaBonte, "Structure and energy of one-dimensional domain walls in ferromagnetic thin films," *J. Appl. Phys.*, vol. 36, no. 4, pp. 1380–1386, Apr. 1965, doi: 10.1063/1.1714314.

[5] A. E. LaBonte, "Two-dimensional bloch-type domain walls in ferromagnetic films," *J. Appl. Phys.*, vol. 40, no. 6, pp. 2450–2458, May 1969, doi: 10.1063/1.1658014.

[6] D. Jiles, *Introduction to Magnetism and Magnetic Materials*. London, U.K.: Chapman & Hall, 1991.

[7] A. S. Lileev et al., "The Effects of Thermomagnetic Treatment on the Magnetic Properties of Nanocrystalline Fe–O and Fe-Co–O Pressed Compacts," *J. Supercond. Novel Magn.*, vol. 38, pp. 1–9, 2025, doi: 10.1007/s10948-024-06837-z.

[8] R. M. Bozorth, *Ferromagnetism*. New York, NY, USA: IEEE Press, IEEE Magnetics Society, The Institute of electrical and Electronics Engineers, 1993.

[9] S. Chikazumi, *Physics of Ferromagnetism*, 2nd ed., Oxford, U.K.: Clarendon Press, 1997.

[10] B. G. Lifshitz, V. S. Kraposhin, and Y. L. Linetskyi, *Physical Properties of Metals and Alloyes*. Moscow, Russia: Metallurgie, 1989.

[11] A. S. Lileev, "Effect of magnetostatic interaction between microvolumes on the formation of the domain structure and reversal of magnetization in $Sm(Co,Fe,Cu,Zr)_{7.5}$ alloy," *Bull. Russian Acad. Sci., Phys.*, vol. 86, no. 5, pp. 584–587, May 2022, doi: 10.3103/s1062873822050161.

[12] M. Schabes and A. Aharoni, "Magnetostatic interaction fields for a three-dimensional array of ferromagnetic cubes," *IEEE Trans. Magn.*, vol. MAG-23, no. 6, pp. 3882–3888, Nov. 1987, doi: 10.1109/TMAG.1987.1065775.

[13] A. S. Lileev and V. V. Pinkas, "Phenomenological approach to analyzing the magnetization reversal of uniaxial highly anisotropic ferromagnetic materials," *Bull. Russian Acad. Sci., Phys.*, vol. 83, no. 7, pp. 795–797, Jul. 2019, doi: 10.3103/s1062873819070244.

[14] L. De Los Santos V. et al., "Magnetic measurements of suspended functionalised ferromagnetic beads under DC applied fields," *J. Magn. Magn. Mater.*, vol. 321, no. 14, pp. 2129–2134, Jul. 2009, doi: 10.1016/j.jmmm.2009.01.019.

[15] V. N. Viktorov, A. S. Lileev, A. S. Perminov, B. G. Razumeiko, A. S. Starikova, and E. A. Shuvaeva, *Program of Phenomenological Modeling of the Demagnetization Processes of the Highly Anisotropic Uniaxial Magnetic Materials*, document No.2009612954, Certificate of Computer Program State Registration, Apr. 2009.

[16] Y. V. Konyukhov, V. M. Nguyen, and D. I. Ryzhonkov, "Kinetics of reduction of α-Fe_2O_3 nanopowder with hydrogen under power mechanical treatment in an electromagnetic field," *Inorganic Mater., Appl. Res.*, vol. 10, no. 3, pp. 706–712, May 2019, doi: 10.1134/s2075113319030171.

[17] E. H. Lalana, "Imanes permanentes y su Producción por pulvimetalurgia," *Revista de Metalurgia*, vol. 54, no. 2, p. e121, Jun. 2018, doi: 10.3989/revmetalm.121.

[18] K. Takagi, Y. Hirayama, S. Okada, A. Hosokawa, and W. Yamaguchi, "Recent research trend in powder process technology for high-performance rare-Earth permanent magnets," *KONA Powder Part. J.*, vol. 40, pp. 74–93, Jan. 2023, doi: 10.14356/kona.2023007.

[19] E. V. Shelekhov and T. A. Sviridova, "Programs for X-ray analysis of polycrystals," *Metal Sci. Heat Treat.*, vol. 42, no. 8, pp. 309–313, 2000.

[20] H. M. Rietveld, "Line profiles of neutron powder-diffraction peaks for structure refinement," *Acta Crystallogr.*, vol. 22, pp. 151–152, Jan. 1967.

[21] L. De Los Santos Valladares et al., "Preparation and crystallization of hollow α-Fe_2O_3 microspheres following the gas-bubble template method," *Mater. Chem. Phys.*, vol. 169, pp. 21–27, Feb. 2016, doi: 10.1016/j.matchemphys.2015.11.021.

[22] L. De Los Santos Valladares et al., "Characterization and magnetic properties of hollow α-Fe_2O_3 microspheres obtained by sol gel and spray roasting methods," *J. Sci., Adv. Mater. Devices*, vol. 4, no. 3, pp. 483–491, Sep. 2019, doi: 10.1016/j.jsamd.2019.07.004.

[23] L. León et al., "Synthesis and characterization of hollow α-Fe_2O_3 submicron spheres prepared by sol–gel," *Hyperfine Interact.*, vol. 202, nos. 1–3, pp. 131–137, Nov. 2011, doi: 10.1007/s10751-011-0353-1.

[24] N. Randrianantoandro, A. M. Mercier, M. Hervieu, and J. M. Grenèche, "Direct phase transformation from hematite to maghemite during high energy ball milling," *Mater. Lett.*, vol. 47, no. 3, pp. 150–158, Jan. 2001, doi: 10.1016/s0167-577x(00)00227-5.

[25] M. D. Alcalá et al., "Synthesis of nanocrystalline magnetite by mechanical alloying of iron and hematite," *J. Mater. Sci.*, vol. 39, no. 7, pp. 2365–2370, Apr. 2004, doi: 10.1023/b:jmsc.0000019998.78644.74.

[26] M. Sahebari, S. H. Raigan, S. A. S. Ebrahimi, and H. Abdizadeh, "Inception of transformation of hematite to magnetite during mechanical activation: A thermodynamical approach," *Iranian J. Sci. Technol.*, vol. 33, no. 5, pp. 415–424, Jan. 2009. [Online]. Available: https://www.scopus.com/record/display.uri?eid=2-s2.0-76349104568&origin=resultslist

[27] J. Kargin et al., "Thermal-reduction and -oxidation of iron oxide slags generated from rolling mill steel industry," *Heat Treatment Surf. Eng.*, vol. 7, no. 1, Dec. 2025, Art. no. 2494356, doi: 10.1080/25787616.2025.2494356.

[28] C. C. Koch and J. D. Whittenberger, "Mechanical milling/alloying of intermetallics," *Intermetallics*, vol. 4, no. 5, pp. 339–355, Jan. 1996, doi: 10.1016/0966-9795(96)00001-5.

[29] A. S. Lileev, Y. D. Yagodkin, E. N. Grishina, E. S. Khanenya, V. S. Nefedov, and O. I. Popova, "Hard magnetic nanocrystalline alloys of Fe–Fe_2O_3 system," *J. Magn. Magn. Mater.*, vols. 290–291, pp. 1217–1220, Apr. 2005, doi: 10.1016/j.jmmm.2004.11.406.

[30] A. S. Lileev, "Mechanisms of remagnetisation of magnetic materials. Modelling of remagnetisation processes," in *Proc. Defect Diffusion Forum*, 2021, pp. 56–61, doi: 10.4028/www.scientific.net/DDF.410.56.

[31] O. Gutfleisch, M. A. Willard, E. Brück, C. H. Chen, S. G. Sankar, and J. P. Liu, "Magnetic materials and devices for the 21st century: Stronger, lighter, and more energy efficient," *Adv. Mater.*, vol. 23, no. 7, pp. 821–842, 2011, doi: 10.1002/adma.201002180.

[32] D. Fiorani, *Surface Effects in Magnetic Nanoparticles*. Cham, Switzerland: Springer, 2005, doi: 10.1007/b136494.

[33] J. Taurines, F. Martin, P. Rasilo, and A. Belahcen, "Thermodynamically consistent magnetic hysteresis model—Application to soft and hard magnetic materials including minor loops," *IEEE Trans. Magn.*, vol. 60, no. 7, pp. 1–9, Jul. 2024, doi: 10.1109/TMAG.2024.3405644.

Coordenação de Aperfeiçoamento de Pessoal de Nível Superior (CAPES) - ROR identifier: 00x0ma614